Title

Dynamic signatures of electronically nonadiabatic coupling in sodium hydride: a rigorous test for the symmetric quasi-classical model applied to realistic, ab initio electronic states in the adiabatic representation

Journal

Physical Chemistry Chemical Physics, 24(8)

ISSN

0956-5000

Authors

Talbot, Justin J
Head-Gordon, Martin
Miller, William H
et al.

Publication Date

2022-02-23

DOI

10.1039/d1cp04090a

PCCP

ARTICLE TYPE

Cite this: DOI: 00.0000/xxxxxxxxxx

Dynamic signatures of electronically nonadiabatic coupling in sodium hydride: a rigorous test for the symmetric quasi-classical model applied to realistic, *ab initio* electronic states in the adiabatic representation†

Justin J. Talbot,*[a] Martin Head-Gordon,[a,b], William H. Miller[a], and Stephen J. Cotton,[a]

Received Date
Accepted Date

DOI: 00.0000/xxxxxxxxxx

Sodium hydride (NaH) in the gas phase presents a seemingly simple electronic structure making it a potentially tractable system for the detailed investigation of nonadiabatic molecular dynamics from both computational and experimental standpoints. The single vibrational degree of freedom, as well as the strong nonadiabatic coupling that arises from the excited electronic states taking on considerable ionic character, provides a realistic chemical system to test the accuracy of quasi-classical methods to model population dynamics where the results are directly comparable against quantum mechanical benchmarks. Using a simulated pump-probe type experiment, this work presents computational predictions of population transfer through the avoided crossings of NaH via symmetric quasi-classical Meyer-Miller (SQC/MM), Ehrenfest, and exact quantum dynamics on realistic, *ab initio* potential energy surfaces. The main driving force for population transfer arises from the ground vibrational level of the $\mathbf{D}^1\Sigma^+$ adiabatic state that is embedded in the manifold of near-dissociation $\mathbf{C}^1\Sigma^+$ vibrational states. When coupled through a sharply localized first-order derivative coupling most of the population transfers between $t = 15$ and $t = 30$ fs depending on the initially excited vibronic wavepacket. While quantum mechanical effects are expected due to the reduced mass of NaH, predictions of the population dynamics from both the SQC/MM and Ehrenfest models perform remarkably well against the quantum dynamics benchmark. Additionally, an analysis of the vibronic structure in the nonadiabatically coupled regime is presented using a variational eigensolver methodology.

1 Introduction

Electronically nonadiabatic processes are ubiquitous throughout many important areas of chemistry.[1–6] From a computational standpoint, dynamic predictions of these processes requires a set of potential energy surfaces, nuclear gradients, and nonadiabatic coupling vectors, as well as a time propagation model for the electronic and nuclear degrees-of-freedom (DOF). One typically prefers analytic gradients for the calculation of nuclear forces and nonadiabatic couplings which provide the greatest accuracy when compared with finite-difference approximations; however, for realistically-sized molecular systems computing analytic gradients and nonadiabatic couplings collectively can amount to by far the dominant computational expense. Over the last decade, *ab initio* electronic structure theory has seen substantial progress in the efficient and accurate calculation of nonadiabatic couplings either through diabatization models[7–11] or directly as a first-order derivative coupling vector in the adiabatic representation.[12–16] However, providing meaningful estimates of nonadiabatic coupling often results in a trade-off between accurate wavefunction-based electronic structure approaches, which can include electron correlation but create a substantial computational cost, or more approximate electronic structure theories which allow for the study of larger systems with higher complexity.

Many dynamics methods have been developed already which can, in principle, utilize an *ab initio* treatment of the electronic structure when propagating the electronic and nuclear

[a]*Department of Chemistry, University of California, Berkeley, California 94720, USA. E-mail: justin.talbot@berkeley.edu*
[b]*Chemical Sciences Division, Lawrence Berkeley National Laboratory, Berkeley, California, 94720, USA.*

† Electronic Supplementary Information (ESI) available: [Additional electronic structure and grid convergence analysis. The linearly-interpolated potential energy surfaces, analytic nuclear gradients, first-order derivative couplings (.xlsx). The calculated vibronic energy levels and select vibronic wavefunctions (.txt).] See DOI: 10.1039/cXCP00000x/

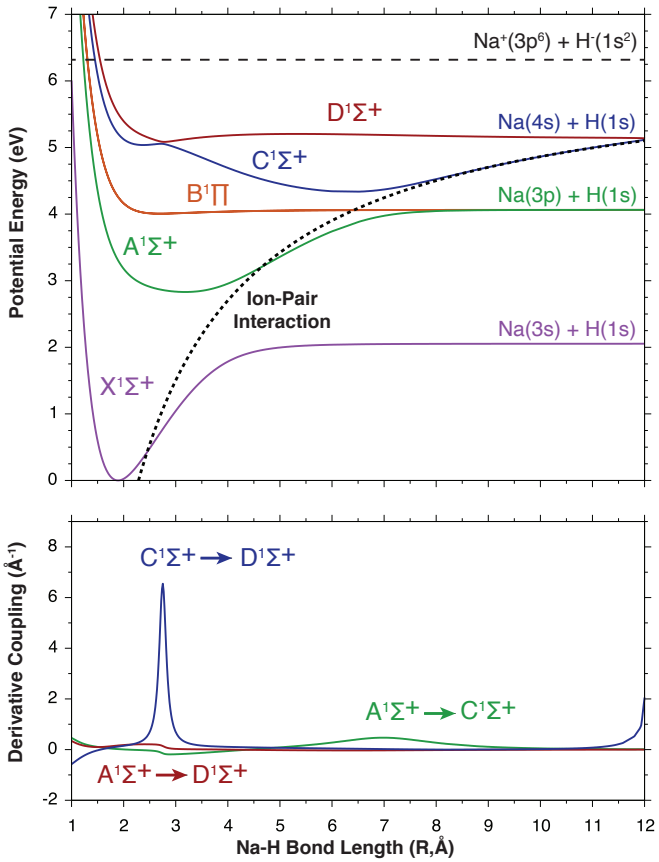

Fig. 1 A comparison between the EOM-EE-CCSD singlet potential energy surfaces of sodium hydride and the ion-pair interaction energy. The dashed line at 6.303 eV is the calculated ion-pair dissociation limit (**top**). The calculated bond length dependence of the first-order derivative couplings between the excited singlet states (**bottom**). There are two avoided crossings between the **C**-**D** potential energy surfaces (blue). The first avoided crossing (**R**=2.72Å) has the strongest, but most localized, first-order derivative coupling. The second avoided crossing (**R**≈12Å) is weaker in comparison but causes the **C** state to dissociate at the Na(4s)+H(1s) limit. The first-order derivative coupling between **A**-**C** (green) and the **A**-**D** potential energy surfaces (brown) is also shown.

DOF. Some of these methods include FSSH[17–19], Ehrenfest[20–24], AIMS[25–28], and SQC/MM[29,30], which all involve different approximations and cost trade-offs.[31,32] Ideally, one would choose a quantum mechanical-based method for both the electronic and nuclear dynamics which generally offers the greatest accuracy. However, as these methods scale exponentially with system size they are typically prohibitively expensive for all but the lowest-dimensional chemical systems.[33–35] When true quantum mechanical effects, e.g., tunneling, are not too important treating the electronic and/or nuclear DOF with classical mechanics offers an appealing low cost alternative with easily parallelizable trajectories that are directly amenable to electronic structure calculations.

The symmetric quasi-classical Meyer-Miller (SQC/MM) approach is in essence a simple quantization model used in conjunction with the classical electronic+nuclear dynamics arising from the Meyer-Miller (MM) Hamiltonian. While maintaining a foundation that is based entirely in classical mechanics, SQC/MM has predicted with reasonable accuracy a wide range of electronically nonadiabatic processes for many model systems including site-exciton and spin-boson models,[36–41] simple Tully models,[42–44] and, related to the present study, a Morse potential model of dissociation dynamics[45]. While the treatment of model chemical systems with SQC/MM have oftentimes been demonstrated in the diabatic representation, for *ab initio* simulations the natural representation is in terms of the adiabatic electronic states arising from the Born-Oppenheimer approximation. Recent years have seen significant progress in the development and application of SQC/MM to study general molecular systems in the adiabatic basis where potential energy surfaces, nuclear gradients, and nonadiabatic coupling vectors are calculated "on-the-fly" using available electronic structure theories.[46–50] Pushing these ideas further, demonstrative calculations of the SQC/MM model where the results are readily comparable against experimental measurements and/or quantum mechanical benchmarks, represents another step towards the development of a sufficiently accurate "black box" approach for predicting the nonadiabatic dynamics of general molecular systems.

Alkali hydrides are some of the simplest diatomic molecules which may serve as realistic *ab initio* test systems for studying the accuracy of the SQC/MM model. Their ground electronic states ($\mathbf{X}^1\Sigma^+$) are primarily single configurational with energies well-separated from their excited electronic states. Likewise, their deep potential wells lend themselves to small anharmonicity constants where calculations of ground state properties qualitatively reproduce experimental observations even with crude theoretical models.[51–55] In their excited electronic states, these seemingly simple systems gain substantial complexity as their electronic structure at longer bond lengths takes on a considerable amount of ionic character.[56,57] This, in turn, introduces a cascade of avoided crossings between the excited Born-Oppenheimer potential energy surfaces. Since the low-lying electronic states of these systems are generally well-described with only single and double excitations, in a manageable active space, they are also prime candidates for the use of accurate wavefunction theories like equation-of-motion coupled cluster theory with single and double excitations (EOM-EE-CCSD). The benefit of using such a high level of electronic structure theory for a such simple systems is that a realistic description of the underlying potential energy surfaces may be obtained along with analytic gradients for the calculation of nuclear forces and nonadiabatic derivative-coupling vectors.[58–60]

While to some degree all of the alkali hydrides exhibit this series of avoided crossings, a prime example is seen in the excited potential energy surfaces of sodium hydride (see Fig. 1).[61,62] The relatively low-energy ion-pair dissociation limit, $Na^+(3p^6)$ + $H^-(1s^2)$, introduces significant anharmonicity along the **A**, **C**, and **D** $^1\Sigma^+$ potential energy surfaces as their outer wells take on a substantial amount of ionic character.[62] For the **A** electronic state, the ionic contribution extends the outer well to long bond lengths, in effect, forming a shallow potential well that dissociates at the Na(3p) + H(1s) limit. As the ion-pair dissociation limit is approached by the **C** and **D** potential energy surfaces however, the ionic character becomes more pronounced forming outer wells of

the **C** and **D** electronic states that are purely ionic. The result, for the **C** and **D** states, is two double-well potential energy surfaces with two avoided crossings ($\mathbf{R}$= 2.72Å, $\mathbf{R}\approx$ 12Å). While the **C** state dissociates at the Na(4s) + H(1s) asymptote, the **D** state continues to follow the ion-pair interaction energy until dissociation at the Na(3d) + H(1s) limit.[†]. Additionally, the displacement of the **C** surface's outer well introduces a far weaker avoided crossing with the **A** surface (see bottom panel of Fig. 1).

Recent studies of sodium hydride have utilized available experimental and theoretical data to fit accurate ground and excited state potential energy surfaces. On the theoretical front, a study by Aymar, Deiglmayr, and Dulieu found that static polarizibilities, transition, and permanent dipole moments could be accurately predicted by modelling the electronic structure of sodium hydride as an effective two-electron system in the full configuration interaction limit—solidifying the use of double excitation methods for an accurate description of electronic properties.[† 61] Later, using these calculations as well as available experimental data, Walji, Sentjens, and Le Roy went on to fit highly accurate potential energy surfaces for the **X** and **A** states capable of producing vibrational lines that are directly comparable to experimental measurements.[62,63] From experiments, a study from Chu, *et al*. found the double-well potential of the **C** state could be accessed using optical-optical double resonance fluorescence spectroscopy.[64,65] After a potential fit analysis, the highest experimentally accessible vibrational level of the **C** state was determined which notably lies directly in the region of strong first-order derivative coupling between the **C** and **D** potential energy surfaces.

The aims of the present study are two-fold. First, electronic structure and vibronic energy levels of the low-lying singlet electronic states of sodium hydride are presented with the hope that these benchmarks could be confirmed through a properly constructed experiment. These predictions were based from EOM-EE-CCSD quality potential energy surfaces, analytic nuclear gradients and first-order derivative couplings, as well as the vibronic eigenstates which were calculated using a variational eigensolver. Second, using these calculations, the accuracy of SQC/MM to model the population dynamics through this series of avoided crossings is evaluated and compared against Ehrenfest predictions and quantum wavepacket benchmarks.

2 Methods

2.1 Electronic Structure

The potential energy surfaces, analytic nuclear gradients, and first-order derivative couplings were calculated using the EOM-EE-CCSD method with the core-valence polarized aug-cc-pCVQZ basis set. The EOM-EE-CCSD excitation energies of NaH, as well as four Rydberg states of the sodium atom were used to assess convergence with respect to basis set. The number of occupied orbitals included in the correlated calculations was determined from convergence tests of the excitation energies evaluated at the ground state equilibrium bond length. Correlation consistency was obtained after omitting the sodium atom's 1*s* electrons from the correlated calculations. Likewise, core-valence polarized basis functions were required to obtain a reasonable agreement with available experimental data for the Rydberg states of the sodium atom. The coupled-cluster expansion was truncated at double excitations as it was found that including a perturbative triples correction to the energy introduced only a slight improvement to the correlation energy of the **X** electronic state at the equilibrium bond length. The results of the convergence tests are provided in the ESI.[†] All potential energy surfaces, analytic nuclear gradients, and first-order derivative couplings were calculated using a release version of the Q-Chem 5.3 software package.[66]

All electronic properties (energies, gradients, and first-order derivative couplings) were calculated on an evenly spaced grid along a normalized Cartesian displacement vector ($\mathbf{Q}$). The grid spacing was chosen as 0.026Å. All first-order derivative coupling vectors were deduced from analytic gradients using Szalay's approach which is the standard method for calculating EOM-EE-CCSD first-order derivative couplings in Q-Chem 5.3.[58,59] While the grid spacing was fine enough to not require analytic gradients for the calculation of nuclear forces, the use of analytic gradients greatly simplifies the calculation of first-order derivative couplings using EOM-EE-CCSD.[58] For a few significantly displaced bond lengths the coupled-cluster equations were non-convergent, and these points were removed from the data set. While there is substantial first-order derivative coupling between the **C** and **D** potential energy surfaces near $\mathbf{R} \approx 12$Å, the grid was truncated as convergence was particularly problematic in this region. With the converged scan, all interior points were evaluated by interpolation using a linear spline with a 0.015Å grid spacing. Additional convergence tests with respect to grid size, as well as the bond length and $\mathbf{Q}$ dependence of the potential energy surfaces, nuclear gradients, first-order derivative couplings, and select vibrational wavefunctions are provided in the ESI.[†]

2.2 Time-Independent Eigensolver

In order to include the effects of first-order derivative coupling on the vibrational energy levels, the vibronic Schrödinger equation[4] was solved numerically using a modified Fourier-grid[67] variational eigensolver and the Hamiltonian shown in Eq 1:

$$\hat{\mathbf{H}}_{ij} = \frac{1}{2\boldsymbol{\mu}} \left(\hat{\mathbf{P}} - i\hbar\mathbf{d}(\mathbf{Q})\right)^2_{ij} + E_i(\mathbf{Q})\delta_{ij} \tag{1}$$

Conwhere $\boldsymbol{\mu}$ is the reduced mass, $\hat{\mathbf{P}}_{ij} = -i\hbar\delta_{ij}\vec{\nabla}_{\mathbf{Q},\mathbf{Q}'}$ is the momentum operator expressed in the position representation, $\mathbf{d}(\mathbf{Q})$ is a skew-symmetric matrix of first-order derivative coupling vectors, and $E_i(\mathbf{Q})$ is the potential energy surface corresponding to adiabatic state i. The vector-matrix $\mathbf{d}(\mathbf{Q})$ has elements $\mathbf{d}_{ij}(\mathbf{Q}) \equiv \langle\Phi_i|\boldsymbol{\nabla}_{\mathbf{Q}}\Phi_j\rangle$ which are defined as the elements of the first-order derivative coupling vector between adiabatic Born-Oppenheimer electronic states Φ_i and Φ_j after projection onto the normalized displacement coordinate $\mathbf{Q}$. The momentum operator ($\hat{\mathbf{P}}_{ij}$) was transformed from its diagonal momentum representation to the position representation using a forward and reverse Fourier transform accordingly.[67] Solutions to the vibronic Schrödinger equation were computed variationally by expanding the eigenstates in the direct-product adiabatic basis shown in Eq. 2:

$$\Psi(\mathbf{r},\mathbf{Q}) = \sum_i \Phi_i(\mathbf{r},\mathbf{Q})\chi_i(\mathbf{Q}) \tag{2}$$

where $\chi_i(\mathbf{Q})$ is the nuclear contribution to the adiabatic Born-Oppenheimer electronic state $\Phi_i(\mathbf{r},\mathbf{Q})$. The **A**, **C**, and **D** potential energy surfaces, and all corresponding first-order derivative couplings (see bottom panel of Fig. 1), were included in the eigensolver calculation since coupling to the $\mathbf{B}^1\Pi$ state is symmetry forbidden. Due to the substantial grid size, integration of the potential energy surfaces and first-order derivative couplings required in total 2103 basis functions with 701 basis functions attributed directly to each adiabatic state. For reference, the ground vibronic energy (**X**,0) was calculated separately. The Hamiltonian matrix was built and diagonalized using in-house code outside of Q-Chem. Adiabatic only calculations were performed using the same code by setting all matrix-vector elements $\mathbf{d}_{ij}(\mathbf{Q}) = 0$.

2.3 SQC/MM Nonadiabatic Dynamics

The SQC/MM approach to simulating nonadiabatic dynamics combines the classical Hamiltonian of Meyer and Miller (MM) with a simple symmetrical quasi-classical (SQC) quantization procedure for defining the electronic state occupations and other observables.

In brief, the classical MM Hamiltonian[24] maps the electronic DOF in a nonadiabatic process to a collection of classical harmonic oscillators, one for each of the electronic states. In a diabatic representation, it is given by

$$H(\mathbf{x},\mathbf{p},\mathbf{Q},\mathbf{P}) = \frac{1}{2\boldsymbol{\mu}}\mathbf{P}^2 + \sum_i^F \left(\tfrac{1}{2}p_i^2 + \tfrac{1}{2}x_i^2 - \gamma_i\right) H_{ii}(\mathbf{Q}) + \sum_{i<j}^F (p_i p_j + x_i x_j) H_{ij}(\mathbf{Q}), \tag{3}$$

where $\{x_i, p_i\}$ are the coordinates and momenta of the "electronic oscillators" corresponding to a set of F electronic states, $\mathbf{Q}$, $\mathbf{P}$ are the coordinates and momenta of the nuclear DOF having reduced masses $\boldsymbol{\mu}$, $\{H_{ij}(\mathbf{Q})\}$ is an $F\times F$ nuclear coordinate-dependent electronic matrix (diabatic in Eq. 3), and $\{\gamma_i\}$ are a set of zero point energy (ZPE) parameters which are initially adjusted per DOF as noted below. The evolution of the F classical oscillators in Eq. 3 thus describes the electronic configuration in the MM model and, in particular, the classical actions associated with each oscillator

$$n_i \equiv \tfrac{1}{2}p_i^2 + \tfrac{1}{2}x_i^2 - \gamma_i, \tag{4}$$

represent the electronic occupations. The actions $\{n_i\}$ are specifically what are quantized via the SQC windowing protocol[29,30], by multiplicatively weighting the potential energy surfaces, $\{H_{ii}(\mathbf{Q})\}$ in Eq. 3, they determine the effective forces on the nuclei.

In realistic simulations employing rigorous *ab initio* electronic structure theory, the resulting electronic states are adiabatic and, in the adiabatic representation, the MM Hamiltonian is given by

$$\mathbf{H}(\mathbf{x},\mathbf{p},\mathbf{Q},\mathbf{P}) = \frac{1}{2\boldsymbol{\mu}}\left(\mathbf{P} + \Delta\mathbf{P}(\mathbf{x},\mathbf{p},\mathbf{Q})\right)^2 + V_{\text{eff}}(\mathbf{x},\mathbf{p},\mathbf{Q}), \tag{5}$$

where $\mathbf{P}$ is still a vector of canonical nuclear momenta but now arises in combination with a nonadiabatic coupling vector potential given by

$$\Delta\mathbf{P}(\mathbf{x},\mathbf{p},\mathbf{Q}) = \sum_{i<j}^F (x_i p_j - x_j p_i)\,\mathbf{d}_{ij}(\mathbf{Q}), \tag{6}$$

which depends explicitly on the standard first-derivative nonadiabatic coupling vector $\mathbf{d}_{ij}(\mathbf{Q}) \equiv \langle \Phi_i | \boldsymbol{\nabla}_{\mathbf{Q}} \Phi_j \rangle$ between adiabatic Born-Oppenheimer electronic states Φ_i and Φ_j (the electronic oscillator variables $\{x_i, p_i\}$ now corresponding to adiabatic electronic states). Eq. 5 also expresses the adiabatic MM Hamiltonian in terms of a symmetrized, occupation-weighted potential

$$V_{\text{eff}}(\mathbf{x},\mathbf{p},\mathbf{Q}) = \frac{1}{F}\sum_i^F E_i(\mathbf{Q}) + \frac{1}{F}\sum_{i<j}^F \left(n_i - n_j\right)\left(E_i(\mathbf{Q}) - E_j(\mathbf{Q})\right), \tag{7}$$

which is commonly employed in both adiabatic and diabatic calculations and guarantees the electronic dynamics are independent of energy scale. Of course, Eq. 7 only references the diagonal elements of the electronic matrix $\{E_i(\mathbf{Q}) \equiv H_{ii}(\mathbf{Q})\}$ because it is diagonal in the adiabatic representation.

Applying Hamilton's equations to Eqs. 5, 6, and 7 yields dynamically-consistent classical EOM for both nuclear and electronic DOF in terms of the canonical coordinates and momenta appearing in Eq. 5 but, unfortunately, will explicitly require the use of *second*-derivative nonadiabatic coupling *matrices* which are extremely impractical to calculate in a simulation employing realistic quantum chemistry for the electronic states (and not readily available in standard codes). The simple cure[46] is to re-write the canonical EOM in terms of a *kinematic* momentum, which results in kinematic EOM which contain only the first-derivative couplings $\mathbf{d}_{ij}$ but are nevertheless exactly equivalent; these kinematic EOM therefore represent the operational formulation employed exclusively in this work:

$$\dot{x}_i = p_i \frac{1}{F}\sum_j^F (E_i(\mathbf{Q}) - E_j(\mathbf{Q})) + \sum_j^F x_j \mathbf{d}_{ji}(\mathbf{Q}) \cdot \frac{\mathbf{P}_{\text{kin}}}{\mu}, \tag{8a}$$

$$\dot{p}_i = -x_i \frac{1}{F}\sum_j^F (E_i(\mathbf{Q}) - E_j(\mathbf{Q})) + \sum_j^F p_j \mathbf{d}_{ji}(\mathbf{Q}) \cdot \frac{\mathbf{P}_{\text{kin}}}{\mu}, \tag{8b}$$

$$\dot{\mathbf{Q}} = \frac{\mathbf{P}_{\text{kin}}}{\mu}, \tag{8c}$$

$$\dot{\mathbf{P}}_{\text{kin}} = -\frac{\partial V_{\text{eff}}}{\partial \mathbf{Q}} - \sum_{ij}\left(\frac{1}{2}p_i p_j + \frac{1}{2}x_i x_j\right)(E_j(\mathbf{Q}) - E_i(\mathbf{Q}))\mathbf{d}_{ij}(\mathbf{Q}). \tag{8d}$$

In the SQC/MM approach, quantization of the classical Hamiltonian dynamics produced by Eq. 8 is accomplished, initially and finally, by Monte Carlo sampling initial actions from a "windowing" function defined by the SQC model and, after running the dynamics for a prescribed time interval (via Eq. 8), "binning" the final actions by a symmetric windowing function. In this work, the triangle windowing model was chosen in combination with the γ-adjustment procedure, exactly as described in Ref. 45, ex-

cept that here the adiabatic version of the MM Hamiltonian is employed through the EOM of Eq. 8. The key point of the γ-adjustment procedure is to set the $\{\gamma_i\}$ in Eq. 4 (and therefore in Eq. 7), per DOF (and per trajectory), so that, for each trajectory, the initial force on the nuclei is that of the initial pure quantum state—i.e., the single-surface force. With this prescription, the $\{\gamma_i\}$ still give the ensemble of trajectories an average ZPE of $\frac{1}{3}$ over the window function which, as described in the SQC/MM papers, is optimal in this model and somewhat less than the quantum value of $\frac{1}{2}$. Again, an important consequence of the SQC model in combination with the γ-adjustment protocol is that the nuclei are subject to ZPE fluctuations (in the forces from the electronic DOF) but that the dynamics is initiated with exactly single-surface pure state forces corresponding to the initially excited adiabatic quantum state.

2.4 Population Dynamics Simulations

The quantum/quasi-classical population dynamics on the coupled **A**, **C**, and **D** states were simulated assuming a pump-probe type experiment. The simulated experimental setup is as follows. At time $t = 0$, a pump laser promotes the **X** ground vibronic state (**X**, $\chi = 0$), calculated either from the vibronic Schrödinger equation (quantum) or as the harmonic oscillator ground vibrational state (quasi-classical) to the **A** potential energy surface which is then allowed to propagate for a delay time δ. At select pump-probe time delays, between $0-250$ fs, the pumped quantum wavepacket or classical particle moving on the **A** potential energy surface is promoted with a probe laser to either the **C** or **D** potential energy surfaces and allowed to further propagate. Finally, quantum and quasi-classical population dynamics are recorded as the wavepacket or classical particle moves through the avoided crossing region between the **C** and **D** adiabatic states. Although the electronic transition dipole moments between the $\mathbf{A} \rightarrow \mathbf{C}$ and $\mathbf{A} \rightarrow \mathbf{D}$ transitions depend on bond length,[61] the population dynamics were simulated assuming both excitations are equally possible—for all pump-probe time delays—in order to better illustrate the strengths and limitations of the Ehrenfest and SQC/MM models.

Using the computed vibronic energy levels, obtained by diagonalization of the Hamiltonian in Eq. 1, quantum wavepacket dynamics were simulated by expanding the probed wavepacket as a linear combination of the nonadiabatically coupled eigenstates and this basis was propagated analytically by solving the time-dependent Schrödinger equation. Quantum dynamics were performed, at each pump-probe delay time, for $t = 60$ fs with a 0.1 fs time step. Since the normalization of the wavepacket is a conserved quantity, the electronic state populations as a function of time were evaluated as the summed contribution to the total norm from each adiabatic basis function Φ_i.

The Ehrenfest and SQC/MM dynamics were simulated by initially sampling $25,000$ nuclear positions and momentum directly from a $0K$ harmonic oscillator Wigner distribution. The reduced mass ($\mu = 1.050$ amu) and harmonic frequency ($\omega = 1162.88$ cm^{-1}) were calculated from the equilibrium bond length of the ground electronic state of NaH. Coupled-cluster with single and double excitations and the aug-cc-pCVQZ basis set was used to calculate the harmonic frequency, reduced mass, and displacement vector **Q**. The Wigner sampled positions and momenta were allowed to propagate classically on the **A** potential energy surface, with a 0.1 fs time step for a time delay δ, before being instantaneously promoted to the **C** or **D** potential energy surfaces where the particle was allowed to further propagate via Meyer-Miller multi-surface dynamics for $t = 60$ fs with the same 0.1 fs time step. The nuclear equations of motion were integrated numerically with a traditional velocity-Verlet integrator and a semi-analytic, direct diagonalization scheme was used to integrate the equations of motion for the electronic action variables. All dynamic simulations were performed using in-house code outside of Q-Chem. The Ehrenfest simulations were performed with the same code by setting $\gamma = 0$.

Table 1 A comparison between select adiabatic ($\mathbf{d}_{ij}(\mathbf{Q}) = 0$) and nonadiabatically coupled vibronic energy levels and their assignments. Each nonadiabatically coupled eigenstate was assigned to a single vibrational level (χ_i) on a single adiabatic potential energy surface (Φ_i) by taking the maximum squared projection.

State (Φ_i, χ_i)	Adiabatic (eV)	Nonadiabatic (eV)	Character
	$X^1\Sigma^+$		
X,0	0.072	0.072	1.000
	$A^1\Sigma^+$		
A,0	2.850	2.850	1.000
A,1	2.888	2.888	1.000
A,2	2.928	2.928	1.000
A,3	2.969	2.969	1.000
A,4	3.011	3.011	1.000
A,5	3.054	3.054	1.000
A,6	3.097	3.097	1.000
A,7	3.141	3.141	1.000
A,8	3.184	3.184	1.000
	$C^1\Sigma^+$		
C,34	5.037	5.038	0.981
C,35	5.051	5.053	0.935
C,36	5.061	5.063	0.846
C,37	5.071	5.069	0.882
C,38	5.084	5.083	0.914
C,39	5.098	5.097	0.940
C,40	5.112	5.110	0.842
C,41	5.126	5.128	0.653
C,42	5.140	5.143	0.742
	$D^1\Sigma^+$		
D,0	5.116	5.116	0.382

3 Results & Discussion

3.1 Vibronic Level Structure

The effect of first-order derivative coupling on the adiabatic vibrational energy levels is shown, for a few selected eigenvalues, in Table 1. The eigenstates were assigned to a single vibrational level χ_i on the **X**, **A**, **C**, or **D** electronic states by taking the maximum squared projection onto the adiabatic basis functions Φ_i,χ_i. The energy zero is set at the bottom of the well of the **X** potential energy surface allowing for direct comparison with Fig. 1. As shown in the table, vibronic states with primarily **A** character maintain their adiabaticitiy—at least for low-lying vibrational

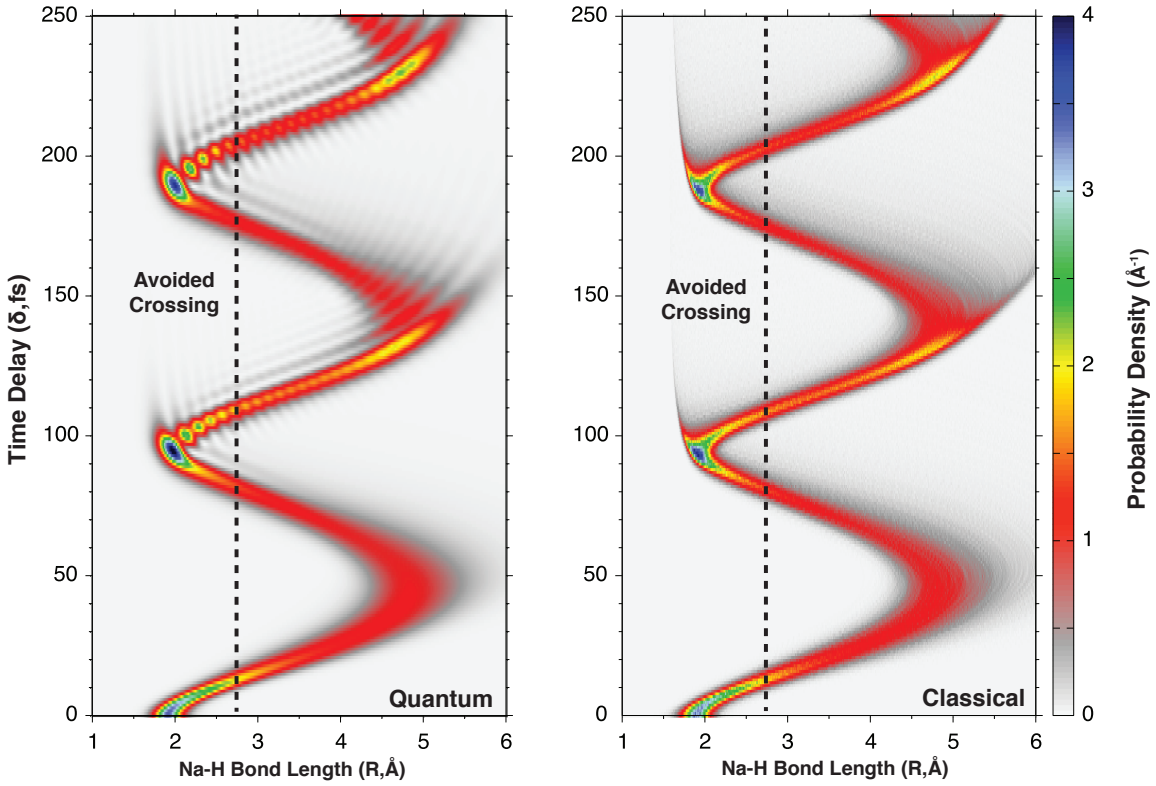

Fig. 2 The pump-probe delay time δ and bond length dependence of the quantum wavepacket (**left**) and the classical trajectories (**right**) propagating along the **A** potential energy surface. The dashed line in both plots is the position of maximum first-order derivative coupling between the **C** and **D** potential energy surfaces.

levels—while the adiabatic character of the highly-excited vibrational levels of the **C** state progressively decreases until the dissociation limit of the **C** potential energy surface is reached.[†]

The first-order derivative coupling between the **A** and **C** potential energy surfaces peaks at $\mathbf{R} \approx 7$Å in bond length with a delocalized spread of nearly ± 2Å (see bottom panel of Fig. 1). This relatively weak coupling, in addition to the even weaker coupling between the **A**-**D** states, introduces minimal mixing with adiabatic states from the **C** and **D** manifolds. As the outer well of the **A** potential energy surfaces takes on substantial ionic character however, the resulting anharmonicity creates a potential where the energetic splitting between vibrational levels slightly increases with vibrational excitation (see Table 1).[62] As a result, the low-lying vibrational eigenstates of the **A** state are delocalized over a wide range of bond lengths. For example, the average bond length of the $\chi = 8$ vibrational level is $\langle \mathbf{R} \rangle = 3.41$Å which is significantly longer than the **X** ($\chi = 0$) ground state which only has an average bond length of $\langle \mathbf{R} \rangle = 1.92$Å.

Although energetically well separated from higher quanta electronic states,[61] the **D** potential energy surface reaches a maximum at $\mathbf{R} = 5.30$Å forming a sufficiently high barrier that localizes low-lying vibrational states at either short or long bond lengths.[†] As a result, the vibronic state with primarily **D**,0 character, localized around shorter bond lengths, actually lies below the dissociation threshold of the **C** potential energy surface. This embedding in the manifold of **C** states, mediated by the strong **C**-**D** first-order derivative coupling, results in a substantial degradation of adiabatic character where the maximum squared projection onto the adiabatic basis function is only 0.382. While adiabatically the **D** potential energy surface supports many higher-energy bound states, when first-derivative coupling is accounted for these states unbind as they mix with continuum states from the **C** manifold.

3.2 $A^1\Sigma^+$ Quantum/Classical Dynamics

The time dependence of the initially excited quantum wavepacket (**X**, $\chi = 0$), propagating along the **A** potential energy surface, is shown in the left panel of Fig. 2. The dashed line indicates the bond length were the first-order derivative coupling between the **C** and **D** states is maximum—which occurs along the repulsive wall of the **A** potential energy surfaces. After initial promotion from the **X** state, there is a spreading that results from anharmonicity as the wavepacket approaches the bottom of the **A** potential well. This spread maximizes between $\mathbf{R} = 4$Å and $\mathbf{R} = 6$Å as the wavepacket nears the classical turning point of the outer well ($\delta \approx 50$ fs). Then, as the inner well is approached from longer bond lengths, a sharp contraction of the wavepacket is observed as it moves up the repulsive wall. For pump-probe delay times longer than 90 fs, the spatial extent of the wavepacket remains mostly intact although nodes are introduced due to further spreading. Throughout the 250 fs pump-probe delay range the wavepacket, moving on the **A** potential energy surface, passes through the avoided crossing region a total of five times—three from the left (shorter bond lengths) and two from the right

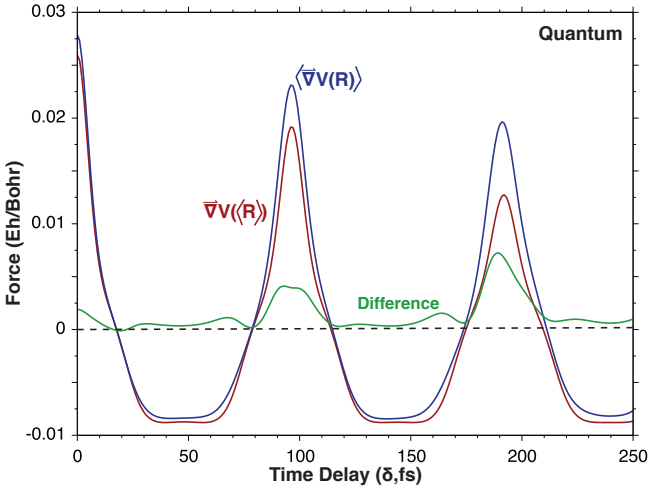

Fig. 3 A comparison between the average force and the force evaluated at the average position of the pumped quantum wavepacket propagating along the **A** potential energy surface as a function of pump-probe delay time δ.

(longer bond lengths).

Remarkably similar dynamics are seen when the motion on the **A** potential energy surface is purely classical and sampled from the $0K$ harmonic oscillator Wigner distribution as shown in the right panel of Fig. 2. The classical motion on the **A** potential energy surface has a comparable spreading to the quantum wavepacket near the outer well, between $\mathbf{R} = 4$Å and $\mathbf{R} = 6$Å, as well as a similar contraction as the particle approaches the repulsive wall near $\mathbf{R} \approx 2$Å. While both quantum and classical dynamics have a comparable period, wavelength, and general form across all pump-probe delay times, the primary distinction between the two approaches is that the quantum wavepacket develops nodes at pump-probe delay times $\delta > 100$ fs which aren't observed in the classical motion.

To investigate the near classical motion of the quantum wavepacket further, comparisons between the classical force averaged over the quantum wavepacket and the classical force evaluated at the quantum wavepacket's average position as a function of pump-probe time delay are provided in Fig. 3. The average force calculations suggest that since the initially excited quantum wavepacket is compact, due to the near-harmonic potential energy surface of the **X** electronic state, quantum motion on the **A** potential energy surface can be approximated, to a reasonable accuracy across all pump-probe delay times, with classical mechanics by Ehrenfest's theorem.

3.3 Nonadiabatic Dynamics

Comparisons between quantum and SQC/MM population dynamics, when the wavepacket is promoted to the **C** state, are shown in the left and middle panels of Fig. 4. The contour lines represent a 0.2 population decrease of the **C** state. Over the 250 fs pump-probe delay range, there are three regions that incur substantial population change ($\delta = 0-20$, $\delta = 70-120$, and $\delta = 160-210$). For pump-probe delay times $\delta < 20$ fs the population transfer is rapid, between $t = 10$ and $t = 25$ fs, ending with less than 0.2 population remaining in the **C** state. There are regions of pump-probe delay times where there is no population change as the wavepacket leaves the nonadiabatically coupled region and approaches the outer well of the **A** potential energy surface. As the wavepacket approaches the avoided crossing from the right, which occurs first near $\delta = 70$ fs, the population transfer is again rapid with most of the population transferring before $t = 10$ fs. Finally, for $\delta > 160$ fs, the introduction of nodes in the wavepacket and the increased spread results in an overall loss of efficiency in population transfer ending with less than 0.3 population remaining in the **C** state after passing through the avoided crossing region.

In general, the signed errors, which are simply defined as the difference between the quantum and SQC/MM populations, are around ± 0.2 for population transfer from the **C** adiabatic state (see right panel of Fig. 4). The contour lines in the error plot represent a change in signed error of ± 0.1 population change. The errors are more pronounced for longer simulation times ($t > 50$ fs), as well as longer pump-probe delay times ($\delta > 160$ fs) with the largest errors occurring, in general, during the final pass through the avoided crossing. While the population transfer estimates with SQC/MM are slightly less efficient when compared with the quantum mechanical simulations, the SQC/MM dynamics do recover the same qualitative trend. For example, there is no population transfer when the initially excited classical particle is out of the nonadiabatically coupled region. Also consistent with the quantum mechanical simulations, the population transfer begins very quickly when the wavepacket approaches the avoided crossing from the left or the right (near $\delta = 80, 110, 170,$ and 200 fs) but is significantly slower when the wavepacket is promoted directly onto the avoided crossing region (near $\delta = 0, 90$ and 185 fs).

Comparisons between population transfer calculated with the Ehrenfest model and the quantum benchmark are provided in Fig. 5. While the signed errors between SQC/MM and Ehrenfest are similar across most pump-probe delay times δ, slightly lower errors are seen with Ehrenfest better estimating population dynamics in the longer time limit ($\delta > 50$ fs) across all three regimes. In fact, for population transfer from the **C** state, errors with the Ehrenfest model are only greater than 0.1 when the avoided crossing is approached from the right ($\delta = 70, 160$ fs). Interestingly, the errors in this region are positive where Ehrenfest tends to systematically overestimate the amount of population transfer compared with SQC/MM. For a clearer comparison of the error, two single cuts through the 2D population maps in Fig. 4 and 5 are shown, for $\delta = 5$ fs and $\delta = 70$ fs, in Fig. 6.

When the wavepacket, or classical particle, is promoted to the **D** state, the population transfer is more efficient overall and occurs over a longer range of pump-probe delay times when compared with promotion to the **C** state. Comparisons between the quantum wavepacket and SQC/MM population dynamics for this case are shown in left and middle panels of Fig. 7. Again, the contour lines represent 0.2 decrease in population of the **D** state. Quantum mechanically the population transfer is very rapid with nearly eighty percent of the population transferring in $t < 15$ fs—substantially shorter than population transfer from the **C** state which takes $t \approx 30$ fs. Also, when initially promoted to the **D** state,

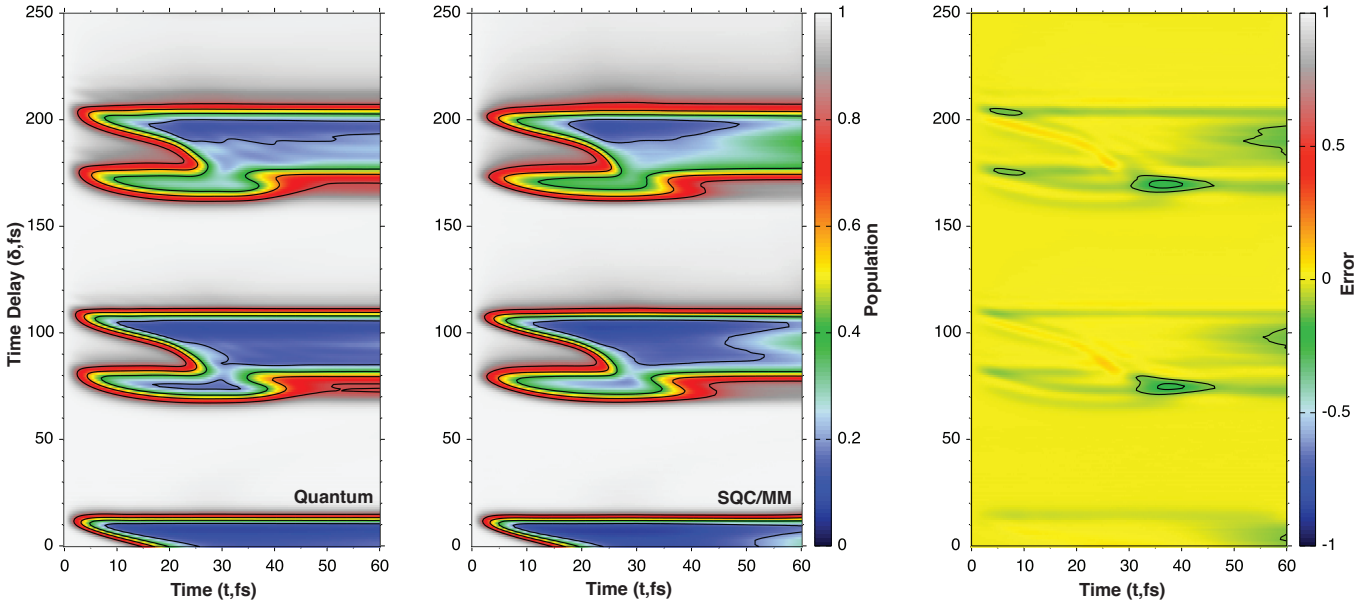

Fig. 4 SQC/MM Dynamics. The population of the **C** adiabatic state after initial excitation from the **A** adiabatic state simulated up to $t = 60$ fs with pump-probe delay times (δ) between $0 - 250$ fs. The populations are calculated from quantum wavepacket dynamics (**left**) and the SQC/MM model (**middle**). The contour lines represent a decrease of 0.2 population in each plot. The calculated signed error between the quantum and SQC/MM results with contour lines representing a signed error of ± 0.1 (**right**).

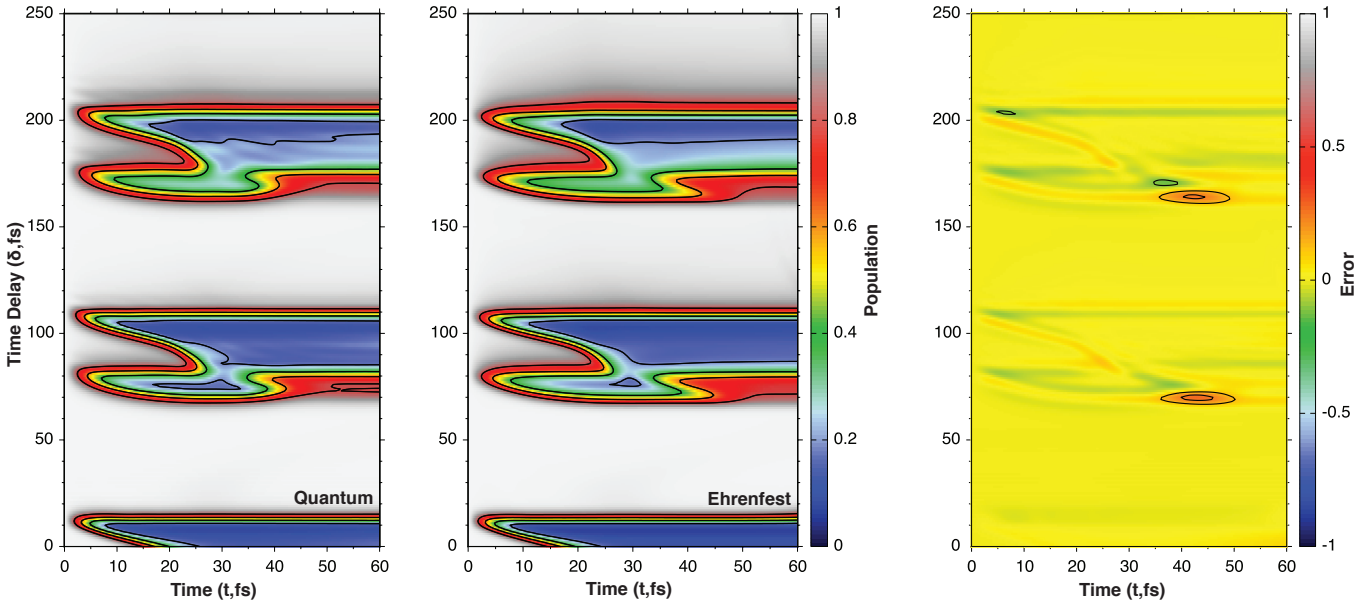

Fig. 5 Ehrenfest Dynamics. The population of the **C** adiabatic state after initial excitation from the **A** adiabatic state simulated up to $t = 60$ fs with pump-probe delay times (δ) between $0 - 250$ fs. The populations are calculated from quantum wavepacket dynamics (**left**) and the Ehrenfest model (**middle**). The contour lines represent a decrease of 0.2 population in each plot. The calculated signed error between the quantum and Ehrenfest results with contour lines representing a signed error of ± 0.1 (**right**).

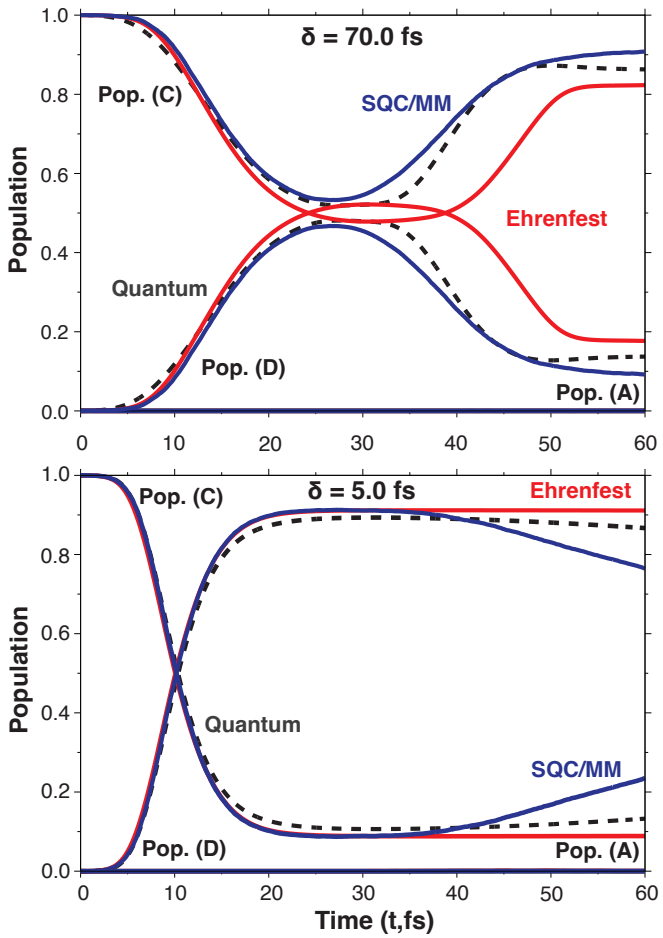

Fig. 6 Population dynamics at select pump-probe delay times ($\delta = 5$ fs (**bottom**) and $\delta = 70$ fs (**top**)) for population transfer from the **C** adiabatic state. Comparisons are made between Ehrenfest predictions (red), SQC/MM predictions (blue), and the quantum benchmark (black).

ranges of pump-probe delay times with no population transfer are shorter compared with population transfer from the **C** state. For longer pump-probe delay times ($\delta > 150$ fs), the population transfer is again less efficient overall when compared with population transfer when $\delta > 50$ fs and is more pronounced when the wavepacket approaches the avoided crossing from the right.

A similar agreement between the quantum mechanical and SQC/MM results is seen for population transfer from the **D** state with SQC/MM predicting population dynamics that are remarkably close to the quantum benchmark. Signed errors for this case are shown in the right panel of Fig. 7. In general, the errors are largest when the avoided crossing is approached from the right but still remain low over all pump-probe delay times. Comparable to the population transfer from the **C** state, the errors progressively worsen at longer pump-probe delay times with the largest errors occurring for $\delta > 150$ fs. When compared with the right panel of Fig. 4, where signed errors of around -0.2 are predicted, signed errors of around -0.1 for this case are observed for pump-probe delay times $\delta > 50$ and $\delta > 150$ fs. Likewise for simulation times $t > 50$ fs, the errors are less than 0.1 across all three relevant ranges of pump-probe delay times.

Comparisons between population transfer from the **D** state calculated with the Ehrenfest model and the quantum benchmark are provided in Fig. 8. The errors with Ehrenfest compared with SQC/MM are remarkably similar for this case with the signed errors less than 0.2 across all pump-probe delay times.

4 Conclusions

In this work, potential energy surfaces and first-derivative couplings calculated at the EOM-EE-CCSD level with a quadruple-zeta quality core-valence polarized basis set were presented for the low-lying singlet states of sodium hydride. The vibronic energy levels of the ground and three excited electronic states were analyzed (**X**, **A**, **C**, and **D**) using a variational eigensolver, directly in the adiabatic basis—which included the effect of first-order derivative coupling. As first-order derivative coupling between the **A**–**C** and **A**–**D** adiabatic potential energy surfaces had a negligible effect on the vibronic eigenstates, the non-adiabatic dynamics were effectively reduced to a coupled electronic two-state problem involving only the **C** and **D** adiabatic states.

To illustrate the coupled dynamics on the **C** and **D** electronic states, as modulated by the nuclear DOF, a pump-probe type experiment was assumed. In this simulated experiment, a quantum/quasi-classical wavepacket, moving along the **A** potential energy surface, was promoted to either the **C** or **D** adiabatic states at selected pump-probe delay times and allowed to further propagate. Using classical trajectories and a quantum wavepacket constructed from the corresponding nonadiabatically coupled vibronic states, the population dynamics were recorded as the promoted wavepacket propagated on the coupled **C** and **D** states. Predictions of population transfer from approximate classical models (Ehrenfest and SQC/MM) were assessed and compared directly against the quantum benchmark. While Ehrenfest had slightly less error overall, signed errors of the population transfer from SQC/MM compared against the quantum benchmark were still less than 0.1 over most pump-probe delay times with signed errors around 0.2 only when the avoided crossing was approached from the right.

While the success of the Ehrenfest model displayed here was directly attributed to the quantum wavepacket maintaining compactness while passing through the **C**-**D** avoided crossing, The Ehrenfest model is only statistically exact for a fixed nuclear trajectory—i.e., when the electronic and nuclear DOF are dynamically-uncoupled. The SQC/MM approach employing the triangle-shaped windowing methodology is statistically exact in the same circumstances, but only for two electronic states. Since the Ehrenfest model works well in the case of NaH, one expects that SQC/MM would also provide a consistently good result. Of course, both Ehrenfest and the SQC/MM methods are approximations when the nuclear motion is dynamically-coupled to the electronic DOF. There isn't any reason why one is going to always strictly outperform the other. One expects, and it has been shown here, that when Ehrenfest is adequate, SQC/MM will also be adequate because the equations of motion are the same and the Ehrenfest trajectories are a strict subset of the SQC ensemble. Of course, in other situations, when Ehrenfest is seen to be quite inadequate, SQC/MM can offer a significant improvement through

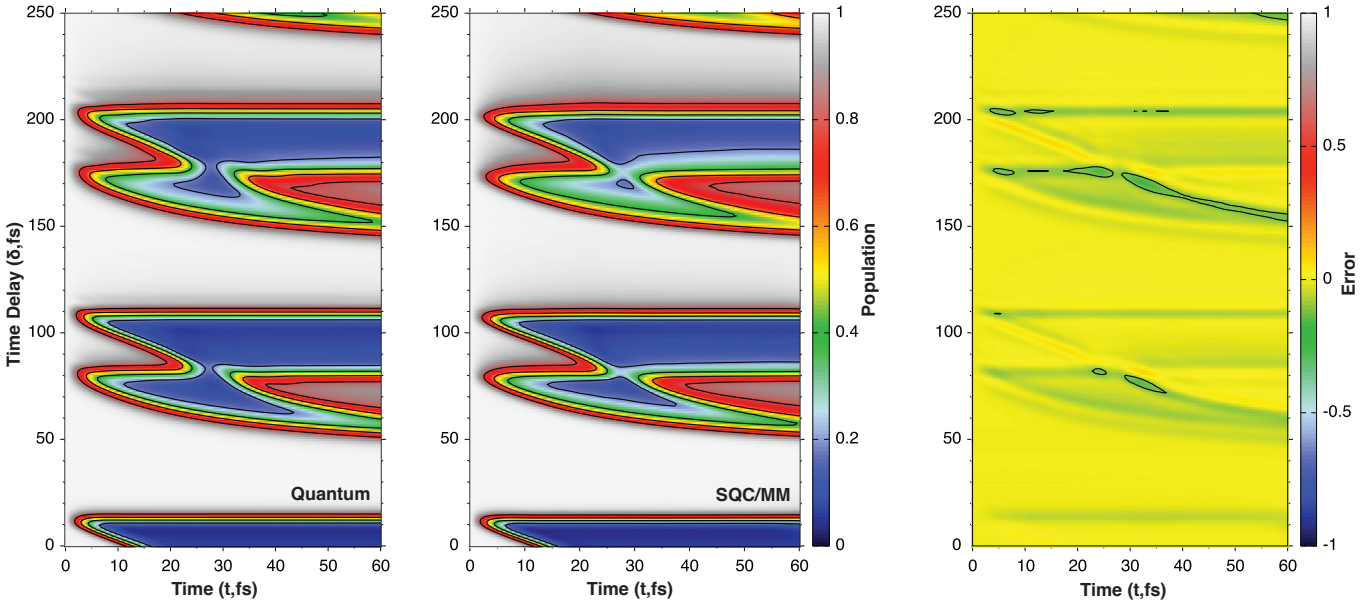

Fig. 7 SQC/MM Dynamics. The population of the **D** adiabatic state after initial excitation from the **A** adiabatic state simulated up to $t = 60$ fs with pump-probe delay times (δ) between $0 - 250$ fs. The populations are calculated from quantum wavepacket dynamics (**left**) and the SQC/MM model (**middle**). The contour lines represent a decrease of 0.2 population in each plot. The calculated signed error between the quantum and SQC/MM results with contour lines representing a signed error of ± 0.1 (**right**).

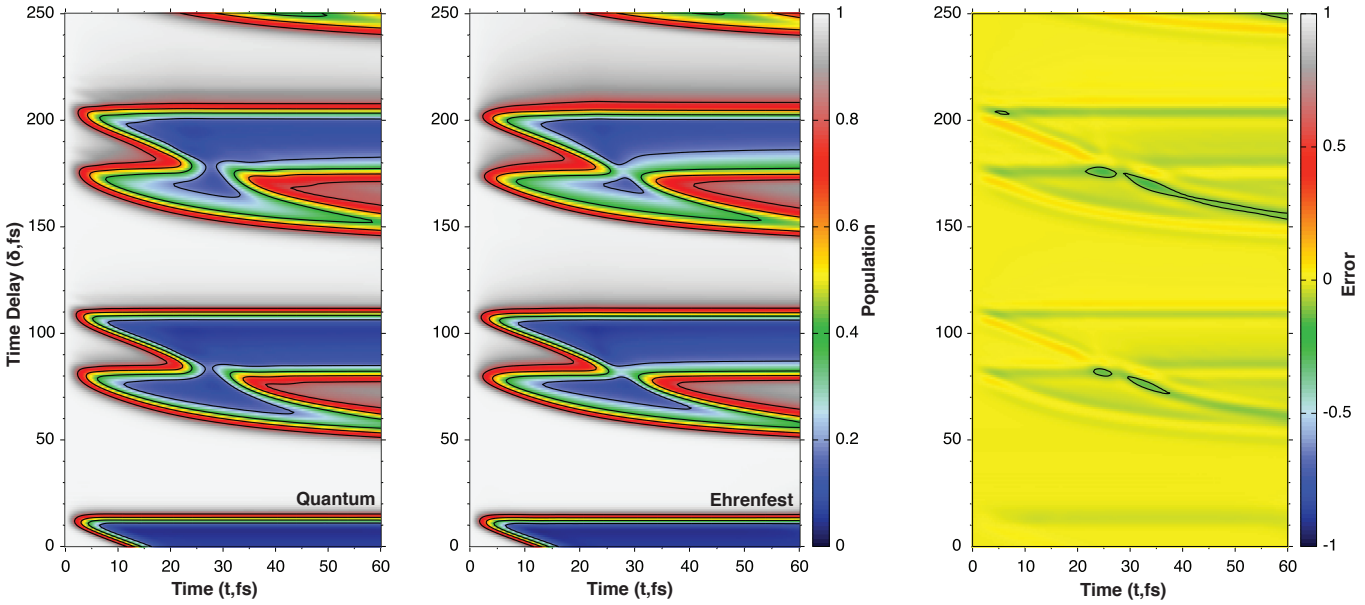

Fig. 8 Ehrenfest Dynamics. The population of the **D** adiabatic state after initial excitation from the **A** adiabatic state simulated up to $t = 60$ fs with pump-probe delay times (δ) between $0 - 250$ fs. The populations are calculated from quantum wavepacket dynamics (**left**) and the Ehrenfest model (**middle**). The contour lines represent a decrease of 0.2 population in each plot. The calculated signed error between the quantum and Ehrenfest results with contour lines representing a signed error of ± 0.1 (**right**).

the systematic and consistent incorporation of an intermediate, but well-tested, level of electronic ZPE.

Conflicts of interest

There are no conflicts to declare.

Acknowledgements

This work is supported by the Director, Office of Science, Office of Basic Energy Sciences of the US Department of Energy under contract No. DE-AC02-05CH11231. This work is supported by the National Science Foundation under grant number CHE-1856707.

References

1 D. R. Yarkony, *Rev. Mod. Phys.*, 1996, **68**, 985.
2 M. S. Schuurman and A. Stolow, *Annual Review of Physical Chemistry*, 2018, **69**, 427–450.
3 B. G. Levine and T. J. Martínez, *Annu. Rev. Phys. Chem.*, 2007, **58**, 613–634.
4 W. Domcke, D. R. Yarkony and H. Köppel, *Conical intersections: theory, computation and experiment*, World Scientific, 2011, vol. 17.
5 A. W. Jasper, C. Zhu, S. Nangia and D. G. Truhlar, *Faraday Discuss.*, 2004, **127**, 1–22.
6 S. Matsika and P. Krause, *Annu. Rev. Phys. Chem.*, 2011, **62**, 621–643.
7 J. E. Subotnik, J. Vura-Weis, A. J. Sodt and M. A. Ratner, *J. Phys. Chem. A.*, 2010, **114**, 8665–8675.
8 Y. Shu and D. G. Truhlar, *J. Chem. Theory Comput.*, 2020, **16**, 6456–6464.
9 Y. Shu, Z. Varga, A. G. Sampaio de Oliveira-Filho and D. G. Truhlar, *J. Chem. Theory Comput.*, 2021, **17**, 1106–1116.
10 Y. Mao, A. Montoya-Castillo and T. E. Markland, *J. Chem. Phys.*, 2020, **153**, 244111.
11 S. L. Li, D. G. Truhlar, M. W. Schmidt and M. S. Gordon, *J. Chem. Phys.*, 2015, **142**, 064106.
12 X. Zhang and J. M. Herbert, *J. Chem. Phys.*, 2014, **141**, 064104.
13 J. E. Subotnik, E. C. Alguire, Q. Ou, B. R. Landry and S. Fatehi, *Acc. Chem. Res.*, 2015, **48**, 1340–1350.
14 S. Fatehi, E. Alguire, Y. Shao and J. E. Subotnik, *J. Chem. Phys.*, 2011, **135**, 234105.
15 S. Fatehi and J. E. Subotnik, *J. Phys. Chem. Lett.*, 2012, **3**, 2039–2043.
16 J. M. Herbert, X. Zhang, A. F. Morrison and J. Liu, *Acc. Chem. Res.*, 2016, **49**, 931–941.
17 J. C. Tully, *J. Chem. Phys.*, 1990, **93**, 1061–1071.
18 L. Wang, A. Akimov and O. V. Prezhdo, *J. Phys. Chem. Lett.*, 2016, **7**, 2100–2112.
19 R. Kapral, *Chem. Phys.*, 2016, **481**, 77–83.
20 X. Li, J. C. Tully, H. B. Schlegel and M. J. Frisch, *J. Chem. Phys.*, 2005, **123**, 084106.
21 F. Ding, J. J. Goings, H. Liu, D. B. Lingerfelt and X. Li, *J. Chem. Phys.*, 2015, **143**, 114105.
22 K. Saita and D. V. Shalashilin, *J. Chem. Phys.*, 2012, **137**, 22A506.
23 C. M. Isborn, X. Li and J. C. Tully, *J. Chem. Phys.*, 2007, **126**, 134307.
24 H.-D. Meyer and W. H. Miller, *J. Chem. Phys.*, 1979, **70**, 3214–3223.
25 B. F. E. Curchod and T. J. Martínez, *Chem. Rev.*, 2018, **118**, 3305–3336.
26 B. F. Curchod, C. Rauer, P. Marquetand, L. González and T. J. Martínez, *J. Chem. Phys.*, 2016, **144**, 101102.
27 M. Ben-Nun, J. Quenneville and T. J. Martínez, *J. Phys. Chem. A*, 2000, **104**, 5161–5175.
28 B. Mignolet and B. F. Curchod, *J. Chem. Phys.*, 2018, **148**, 134110.
29 S. J. Cotton and W. H. Miller, *J. Phys. Chem. A.*, 2013, **117**, 7190–7194.
30 S. J. Cotton and W. H. Miller, *The Journal of chemical physics*, 2013, **139**, 234112.
31 J. C. Tully, *J. Chem. Phys.*, 2012, **137**, 22A301.
32 R. Crespo-Otero and M. Barbatti, *Chem. Rev.*, 2018, **118**, 7026–7068.
33 U. N. Morzan, P. E. Videla, M. B. Soley, E. T. Nibbering and V. S. Batista, *Angew. Chem.*, 2020, **132**, 20219–20223.
34 Y. Kobayashi, K. F. Chang, T. Zeng, D. M. Neumark and S. R. Leone, *Science*, 2019, **365**, 79–83.
35 H. Timmers, X. Zhu, Z. Li, Y. Kobayashi, M. Sabbar, M. Hollstein, M. Reduzzi, T. J. Martínez, D. M. Neumark and S. R. Leone, *Nat. Commun.*, 2019, **10**, 1–8.
36 S. J. Cotton and W. H. Miller, *JCTC*, 2016, **12**, 983–991.
37 Y. Xie, J. Zheng and Z. Lan, *J. Chem. Phys.*, 2018, **149**, 174105.
38 J. Zheng, J. Peng, Y. Xie, Y. Long, X. Ning and Z. Lan, *PCCP*, 2020, **22**, 18192–18204.
39 R. Liang, S. J. Cotton, R. Binder, R. Hegger, I. Burghardt and W. H. Miller, *J. Chem. Phys.*, 2018, **149**, 044101.
40 S. J. Cotton and W. H. Miller, *J. Chem. Phys.*, 2016, **145**, 144108.
41 S. J. Cotton and W. H. Miller, *J. Chem. Phys.*, 2019, **150**, 104101.
42 B. M. Weight, A. Mandal and P. Huo, *J. Chem. Phys.*, 2021, **155**, 084106.
43 S. J. Cotton and W. H. Miller, *J. Phys. Chem. A.*, 2015, **119**, 12138–12145.
44 W. H. Miller and S. J. Cotton, *Faraday Discuss.*, 2017, **195**, 9–30.
45 S. J. Cotton and W. H. Miller, *J. Chem. Phys.*, 2019, **150**, 194110.
46 S. J. Cotton, R. Liang and W. H. Miller, *J. Chem. Phys.*, 2017, **147**, 064112.
47 D. Hu, Y. Xie, J. Peng and Z. Lan, *J. Chem. Theory Comput.*, 2021, 3267–3279.
48 D. Tang, W.-H. Fang, L. Shen and G. Cui, *Phys. Chem. Chem. Phys.*, 2019, **21**, 17109–17117.
49 J. S. Sandoval C, A. Mandal and P. Huo, *J. Chem. Phys.*, 2018, **149**, 044115.

50 W. Zhou, A. Mandal and P. Huo, *J. Phys. Chem. Lett.*, 2019, **10**, 7062–7070.
51 W. C. Stwalley, W. T. Zemke and S. C. Yang, *J. Phys. Chem. Ref. Data*, 1991, **20**, 153–187.
52 S. R. Langhoff, C. W. Bauschlicher Jr and H. Partridge, *J. Chem. Phys.*, 1986, **85**, 5158–5166.
53 H.-Y. Huang, T.-L. Lu, T.-J. Whang, Y.-Y. Chang and C.-C. Tsai, *J. Chem. Phys.*, 2010, **133**, 044301.
54 P. Fuentealba, O. Reyes, H. Stoll and H. Preuss, *J. Chem. Phys.*, 1987, **87**, 5338–5345.
55 A. Belyaev, P. S. Barklem, A. Dickinson and F. Gadéa, *Phys. Rev. A.*, 2010, **81**, 032706.
56 R. W. Numrich and D. G. Truhlar, *J. Phys. Chem.*, 1975, **79**, 2745–2766.
57 N. Khelifi, *J. Phys. Chem. A.*, 2009, **113**, 8425–8433.
58 S. Faraji, S. Matsika and A. I. Krylov, *J. Chem. Phys.*, 2018, **148**, 044103.
59 A. Tajti and P. G. Szalay, *J. Chem. Phys.*, 2009, **131**, 124104.
60 T. Ichino, J. Gauss and J. F. Stanton, *J. Chem. Phys.*, 2009, **130**, 174105.
61 M. Aymar, J. Deiglmayr and O. Dulieu, *Can. J. Phys.*, 2009, **87**, 543–556.
62 S.-D. Walji, K. M. Sentjens and R. J. Le Roy, *J. Chem. Phys.*, 2015, **142**, 044305.
63 T. Rivlin, L. Lodi, S. N. Yurchenko, J. Tennyson and R. J. Le Roy, *Mon. Not. R. Astron. Soc.*, 2015, **451**, 634–638.
64 C.-C. Chu, H.-Y. Huang, T.-J. Whang and C.-C. Tsai, *J. Chem. Phys.*, 2018, **148**, 114301.
65 H.-Y. Huang, Y.-Y. Chang, M.-H. Liao, K.-L. Wu, T.-L. Lu, Y.-Y. Chang, C.-C. Tsai and T.-J. Whang, *Chem. Phys. Lett.*, 2010, **493**, 53–56.
66 Y. Shao, Z. Gan, E. Epifanovsky, A. T. Gilbert, M. Wormit, J. Kussmann, A. W. Lange, A. Behn, J. Deng, X. Feng, D. Ghosh, M. Goldey, P. R. Horn, L. D. Jacobson, I. Kaliman, R. Z. Khaliullin, T. Kuś, A. Landau, J. Liu, E. I. Proynov, Y. M. Rhee, R. M. Richard, M. A. Rohrdanz, R. P. Steele, E. J. Sundstrom, H. L. W. III, P. M. Zimmerman, D. Zuev, B. Albrecht, E. Alguire, B. Austin, G. J. O. Beran, Y. A. Bernard, E. Berquist, K. Brandhorst, K. B. Bravaya, S. T. Brown, D. Casanova, C.-M. Chang, Y. Chen, S. H. Chien, K. D. Closser, D. L. Crittenden, M. Diedenhofen, R. A. D. Jr., H. Do, A. D. Dutoi, R. G. Edgar, S. Fatehi, L. Fusti-Molnar, A. Ghysels, A. Golubeva-Zadorozhnaya, J. Gomes, M. W. Hanson-Heine, P. H. Harbach, A. W. Hauser, E. G. Hohenstein, Z. C. Holden, T.-C. Jagau, H. Ji, B. Kaduk, K. Khistyaev, J. Kim, J. Kim, R. A. King, P. Klunzinger, D. Kosenkov, T. Kowalczyk, C. M. Krauter, K. U. Lao, A. D. Laurent, K. V. Lawler, S. V. Levchenko, C. Y. Lin, F. Liu, E. Livshits, R. C. Lochan, A. Luenser, P. Manohar, S. F. Manzer, S.-P. Mao, N. Mardirossian, A. V. Marenich, S. A. Maurer, N. J. Mayhall, E. Neuscamman, C. M. Oana, R. Olivares-Amaya, D. P. O'Neill, J. A. Parkhill, T. M. Perrine, R. Peverati, A. Prociuk, D. R. Rehn, E. Rosta, N. J. Russ, S. M. Sharada, S. Sharma, D. W. Small, A. Sodt, T. Stein, D. Stück, Y.-C. Su, A. J. Thom, T. Tsuchimochi, V. Vanovschi, L. Vogt, O. Vydrov, T. Wang, M. A. Watson, J. Wenzel, A. White, C. F. Williams, J. Yang, S. Yeganeh, S. R. Yost, Z.-Q. You, I. Y. Zhang, X. Zhang, Y. Zhao, B. R. Brooks, G. K. Chan, D. M. Chipman, C. J. Cramer, W. A. G. III, M. S. Gordon, W. J. Hehre, A. Klamt, H. F. S. III, M. W. Schmidt, C. D. Sherrill, D. G. Truhlar, A. Warshel, X. Xu, A. Aspuru-Guzik, R. Baer, A. T. Bell, N. A. Besley, J.-D. Chai, A. Dreuw, B. D. Dunietz, T. R. Furlani, S. R. Gwaltney, C.-P. Hsu, Y. Jung, J. Kong, D. S. Lambrecht, W. Liang, C. Ochsenfeld, V. A. Rassolov, L. V. Slipchenko, J. E. Subotnik, T. V. Voorhis, J. M. Herbert, A. I. Krylov, P. M. Gill and M. Head-Gordon, *Mol. Phys.*, 2015, **113**, 184–215.
67 C. C. Marston and G. G. Balint-Kurti, *J. Chem. Phys.*, 1989, **91**, 3571–3576.